PNAS RESEARCH ARTICLE | NEUROSCIENCE

Cell type–specific gene therapy confers protection against motor neuron disease caused by a TFG variant

Molly M. Lettman[a], Caitlin A. Mendina[a], Emma Burkard[a], James R. Alvin[a], Yunyun Zhu[a], Joshua J. Coon[a,b,c,d], and Anjon Audhya[a,1]

Affiliations are included on p. 9.

Edited by Craig Blackstone, Massachusetts General Hospital, Boston, MA; received June 1, 2024; accepted October 8, 2024 by Editorial Board Member Peter L. Strick

Inherited forms of motor neuron disease (MND), including hereditary spastic paraplegias (HSP), are associated with the death or dysfunction of nerve cells that control skeletal muscle activity. However, in some cases, the impacts of genetic variants underlying MND act in a non–cell autonomous manner, instead affecting the function of other cell types necessary for neuronal maintenance. Pathological mutations in TFG, which have been implicated in HSP, lead to axonopathy within the corticospinal tract, but it remains unclear whether this problem arises due to perturbations within neurons or supporting neuroglia. To address this question, we leveraged a rat model harboring the recessive TFG p.R106C mutation (mRATBN7.2, g.11:43897639C>T, c.316C>T), which recapitulates multiple phenotypes associated with HSP in humans, including progressive motor deficits, leg spasticity, and indications of an inflammatory response within the motor cortex. In particular, we took advantage of cell type–specific gene therapies to demonstrate that the reintroduction of wild-type TFG into synapsin 1-positive neurons provides robust protection against MND, whereas its expression in GFAP-positive glial cells provides no significant improvement in quantitative measures of gait, despite a dramatic reduction in the presence of reactive astrocytes throughout the brain. These data strongly suggest that therapeutic approaches targeting neurons should be pursued in cases of TFG-HSP, with our animal model offering a unique platform for preclinical assessment.

neuroinflammation | neurodegeneration | spastic paraparesis | SYN1

Degeneration of the corticospinal tract (CST), the main control center for voluntary movement, is characteristic of several motor neuron diseases (MNDs), including hereditary spastic paraplegia (HSP), primary lateral sclerosis (PLS), and amyotrophic lateral sclerosis (ALS) (1, 2). In HSP and PLS, upper motor neurons that originate in layer V of the motor cortex are mainly affected, while in ALS, lower motor neurons with cell bodies in the anterior horn of the spinal cord are additionally impacted (3–6). In all three cases, patients experience progressive weakness and reduced motor control, ultimately limiting their ambulatory functions and severely diminishing quality of life. Despite decades of study, no therapeutic options have been identified to prevent the onset or progression of most MNDs (7–10).

A large number of intrinsic mechanisms are known to facilitate the long-term maintenance of neurons, ranging from ubiquitin-mediated degradation pathways that direct the turnover of damaged proteins and organelles to signaling networks that monitor mitochondrial function and oxidative stress (11–13). Additionally, the microenvironment in which neurons reside enables them to receive support from surrounding cells, including astrocytes, oligodendrocytes, and microglia. In recent years, it has become increasingly clear that impaired function of one cell type in the brain influences the health of its neighbors, and in some cases, the diminished activity of nonneuronal cells can lead to motor neuron degeneration. With respect to MNDs, expression of ALS-associated mutations in astrocytes is toxic to neurons in both cell culture and mouse models, and defects in astrocytic lipid metabolism have been suggested to underlie cortical neuron degeneration in HSP (14–18). Additionally, impaired oligodendrocyte function is sufficient to cause disease phenotypes in mouse HSP models (19, 20). Therefore, defining the cell-autonomous and non–cell autonomous effects of mutations underlying neurodegenerative disease is critical for the development of effective therapeutic options.

Neuronal health is also influenced by neuroinflammation, commonly observed in various forms of neurodegenerative disease and characterized by changes in the density and activity of astrocytes and microglia that release inflammatory signaling molecules (21). The precise relationship between inflammation and neuronal maintenance is unknown

Significance

Hereditary spastic paraplegias (HSPs) are a diverse group of inherited disorders that result in lower limb weakness and spasticity, generally thought to be caused by upper motor neuron degeneration. However, it remains unclear whether axonopathy in HSP arises directly from impaired neuron function or the loss of supporting neuroglia. In this work, we establish a rapid-onset animal model of HSP that recapitulates disease phenotypes exhibited by patients, providing a unique opportunity to test therapeutic interventions. Leveraging cell type–specific gene therapy, we demonstrate that HSP resulting from a hypomorphic mutation in TFG is caused by cell-autonomous neuronal dysfunction. These studies suggest that therapeutic strategies for TFG-HSP should target the cortical neurons that progressively degenerate during the course of disease.

Author contributions: M.M.L., C.A.M., Y.Z., J.J.C., and A.A. designed research; M.M.L., C.A.M., E.B., J.R.A., and Y.Z. performed research; J.J.C. and A.A. contributed new reagents/analytic tools; M.M.L., C.A.M., E.B., J.R.A., Y.Z., and A.A. analyzed data; and M.M.L. and A.A. wrote the paper.

The authors declare no competing interest.

This article is a PNAS Direct Submission. C.B. is a guest editor invited by the Editorial Board.

[1]To whom correspondence may be addressed. Email: audhya@wisc.edu.

This article contains supporting information online at https://www.pnas.org/lookup/suppl/doi:10.1073/pnas.2410996121/-/DCSupplemental.

Published November 11, 2024.

in most cases, and therapies targeting neuroinflammation have had mixed results in cell culture and rodent models, as well as clinical trials for ALS, the best-studied MNDs (22–27). Overall, the immune system assuredly plays a complex role in regulating neurodegeneration, including both protective and detrimental effects during different stages of disease progression, making it a challenging target for therapeutic development (28).

Unlike ALS and PLS, the vast majority of HSP cases are familial and follow clear inheritance patterns, making it an attractive entry point to uncover mechanisms governing MNDs (29–32). Although genetically heterogenous, linked to more than 90 genes, HSP patients consistently present with lower limb spasticity and weakness as a result of upper motor neuron dysfunction, with more complicated forms of the disease additionally exhibiting thinning of the corpus callosum, ventriculomegaly, optic atrophy, and other neurological phenotypes (33–35). Children homozygous for the TFG p.R106C mutation develop complex HSP in their first years of life, and most are unable to move without the use of a wheelchair by adolescence (36–38). Based on our previous work, TFG functions in secretory and endosomal protein trafficking, pathways that both neurons and neuroglia rely on heavily for growth, communication, and survival (39–43). Moreover, animal models harboring the TFG p.R106C mutation exhibit phenotypes closely resembling those of patients, including progressively spastic gait and altered brain morphology (43). To dissect the roles of TFG in neuronal and nonneuronal cells and determine their relative contributions to motor function, we delivered therapeutic adeno-associated viruses to drive long-lasting expression of wild-type (WT) TFG in a cell type–specific manner following a single injection shortly after birth. Strikingly, based on quantitative kinematic analysis, expression of TFG in neurons alone was sufficient to restore normal gait in mutant animals, demonstrating a cell-autonomous role for TFG in neuronal maintenance. Moreover, we establish a rodent model that offers a unique platform to assess the efficacy of future therapeutic approaches, which leverages a significantly shortened analysis timeline relative to other HSP models.

Results

The TFG p.R106C Mutation Diminishes Protein Stability. We demonstrated previously that the presence of the TFG p.R106C mutation is sufficient to cause MNDs associated with progressive gait deficits and thinning of the corpus callosum in Sprague Dawley rats homozygous for the variant, consistent with patient phenotypes (43). These animals exhibit quantifiable disease at ~3 mo of age (43). To aid in the identification and evaluation of potential therapeutics, we sought to accelerate disease onset by reducing gene dosage. To this end, we used CRISPR-Cas9 genome editing to introduce a 17 base pair deletion into exon 4 of the TFG coding sequence, resulting in a premature stop codon immediately after amino acid 108 (Fig. 1*A*). Consistent with prior work, homozygous deletion of TFG resulted in embryonic lethality (41), but compound heterozygous animals harboring one TFG p.R106C allele and one deletion allele ($TFG^{R106C/-}$) were born at normal Mendelian ratios.

To verify reduced gene dosage in $TFG^{R106C/-}$ animals, we conducted bulk RNA sequencing of brain tissue and additionally analyzed brain lysates by quantitative immunoblot. As anticipated, $TFG^{R106C/-}$ animals expressed approximately one-half the number of TFG transcripts as compared to control animals, consistent with the loss of a single allele (Fig. 1*B*). Surprisingly however, levels of TFG protein were reduced by approximately 70% in $TFG^{R106C/-}$ animals as compared to WT controls ($TFG^{+/+}$),

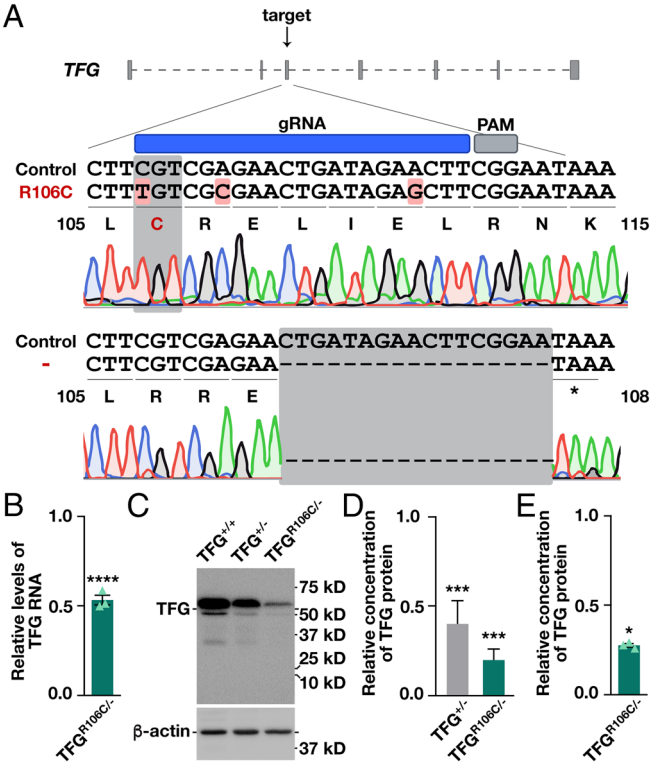

Fig. 1. TFG levels are reduced in $TFG^{R106C/-}$ brain tissue as compared to controls. (*A*) Schematic illustrating the approach used to edit the TFG locus in Sprague Dawley rats (*Top*; gRNA, guide RNA; PAM, protospacer adjacent motif) and chromatograms displaying the DNA sequences of edited animals (*Below*). Nucleotides highlighted red represent changes from the WT sequence, including two silent mutations that were incorporated to facilitate editing. The gray shaded region shows the 17 base pair deletion found in the null allele, leading to creation of an early stop codon (asterisk). Noncoding exon 1 is not shown. (*B*) TFG RNA levels measured by RNA sequencing (n = 3 biological replicates). The error bar represents mean ± SEM. ****$P < 0.0001$, as calculated using a false discovery rate correction for multiple comparisons test. (*C* and *D*) Representative immunoblot (*C*) of brain tissue extracts generated from control and genome-edited animals using antibodies directed against TFG (*Top*) and b-actin (*Bottom*) and subsequent quantification of three biological replicates (*D*). Error bars represent mean ± SEM. ***$P < 0.001$, calculated using ANOVA and post hoc Tukey's multiple comparison tests. (*E*) TFG protein levels measured by mass spectrometry (n = 3 biological replicates). The error bar represents mean ± SEM. *$P < 0.05$, as calculated using a *t* test.

whereas heterozygous null animals (TFG±) expressed approximately one-half the amount of TFG, as expected (Fig. 1 *C* and *D*). To confirm these findings, we measured TFG levels in control and $TFG^{R106C/-}$ animals using whole brain proteomic analysis, which yielded similar results (Fig. 1*E*). Taken together, these data suggest that the p.R106C mutation reduces the stability of TFG in the brain, albeit in a relatively modest manner.

$TFG^{R106C/-}$ Animals Exhibit Rapid Onset and Progression of Motor Dysfunction and Central Nervous System Pathology. To track disease onset and progression in $TFG^{R106C/-}$ animals, we first used kinematic analysis to define two gait parameters, the side-to-side movement of the posterior body (hind body sway) and the height of the tail tip, which we defined previously as early indicators of motor deficits (Fig. 2*A*) (43). In contrast to animals homozygous for the TFG p.R106C mutation, which first display quantifiable gait deficits at approximately 13 wk of age that progress to more severe phenotypes by approximately 25 wk of age (43), $TFG^{R106C/-}$ animals show detectable gait deficits by 6 wk of age and rapidly progress to severe disease by 9 wk of age, with many animals dragging one or both hindlimbs as they cross the platform (Movies S1–S6). Specifically, while there was

no detectable difference between control, TFG±, and TFG$^{R106C/-}$ animals at 3 wk of age, within an additional 3 wk, both male and female TFG$^{R106C/-}$ animals showed an increase in hind body sway, which became more pronounced by 9 wk of age (Fig. 2*B*). Similarly, we found a progressive loss in the ability of TFG$^{R106C/-}$ animals to maintain normal tail tip height, first observed at 6 wk of age for males, and more pronounced (and present in both sexes) at 9 wk of age (Fig. 2*C*). Other gait parameters quantified, including hip height and the angle between the hip, knee, and ankle, failed to reveal dramatic differences between control and mutant animals at 6 wk of age (*SI Appendix*, Fig. S1 *A* and *B*), although there were statistically significant decreases in both parameters at 9 wk of age, which were particularly obvious in TFG$^{R106C/-}$ males (*SI Appendix*, Fig. S1 *A* and *B*).

Overall, we found consistent acceleration of motor dysfunction in TFG$^{R106C/-}$ males relative to females. The exaggerated hind

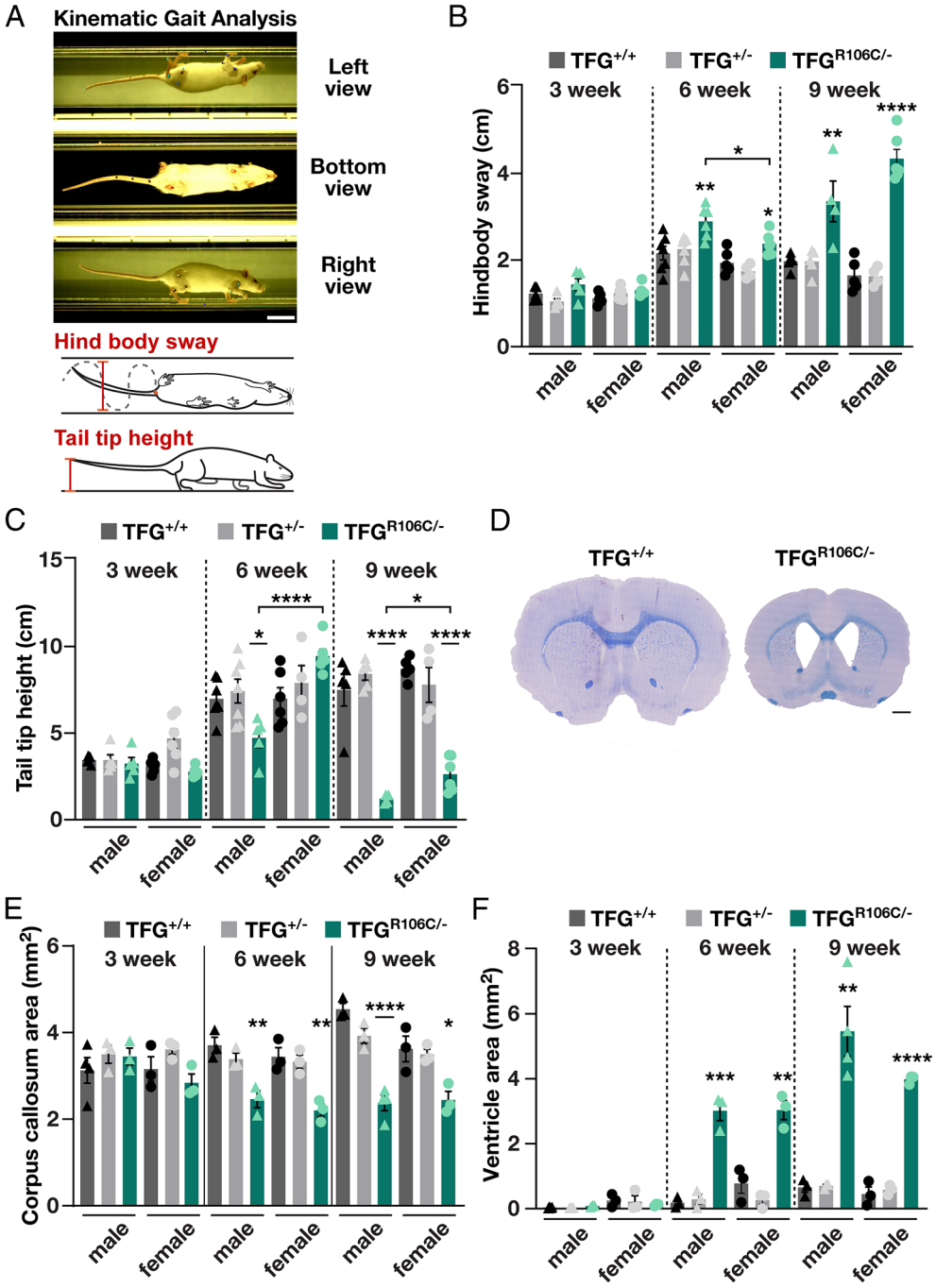

Fig. 2. TFG$^{R106C/-}$ animals exhibit rapid onset motor deficits. (*A*) Representative images from kinematic analysis of a control animal (*Top*; three views). Colored dots represent neural network-tracked body parts and joints. Schematics illustrate the manner in which hind body sway and tail tip height were quantified (*Bottom*). (Scale bar, 5 cm.) (*B* and *C*) Longitudinal measurements of hind body sway (*B*) and tail tip height (*C*) of control and genome-edited animals (4 to 7 animals per group; circles indicate females and triangles represent males). Error bars represent mean ± SEM. *P < 0.05, **P < 0.01, and ****P < 0.0001, as calculated using ANOVA and post hoc Tukey's multiple comparison tests or t tests (indicated by brackets). Statistical evaluations use comparisons relative to control (TFG$^{+/+}$) animals of the same gender, with the exception of t tests, which compare males and females of the same age and genotype. (*D*) Representative luxol fast blue (LFB) stained sections of 9-wk-old control or genome-edited males (n = 3 each). (Scale bar, 1 mm.) (*E* and *F*) Quantification of corpus callosum (*E*) and ventricle area from LFB stained sections of control and genome-edited animals measured over time (3 to 4 animals per group; circles indicate females and triangles represent males). Error bars represent mean ± SEM. *P < 0.05, **P < 0.01, ***P < 0.001, and ****P < 0.0001, as calculated using ANOVA and post hoc Tukey's multiple comparison test. All indications of statistical significance represent comparisons relative to control (TFG$^{+/+}$) animals of the same gender.

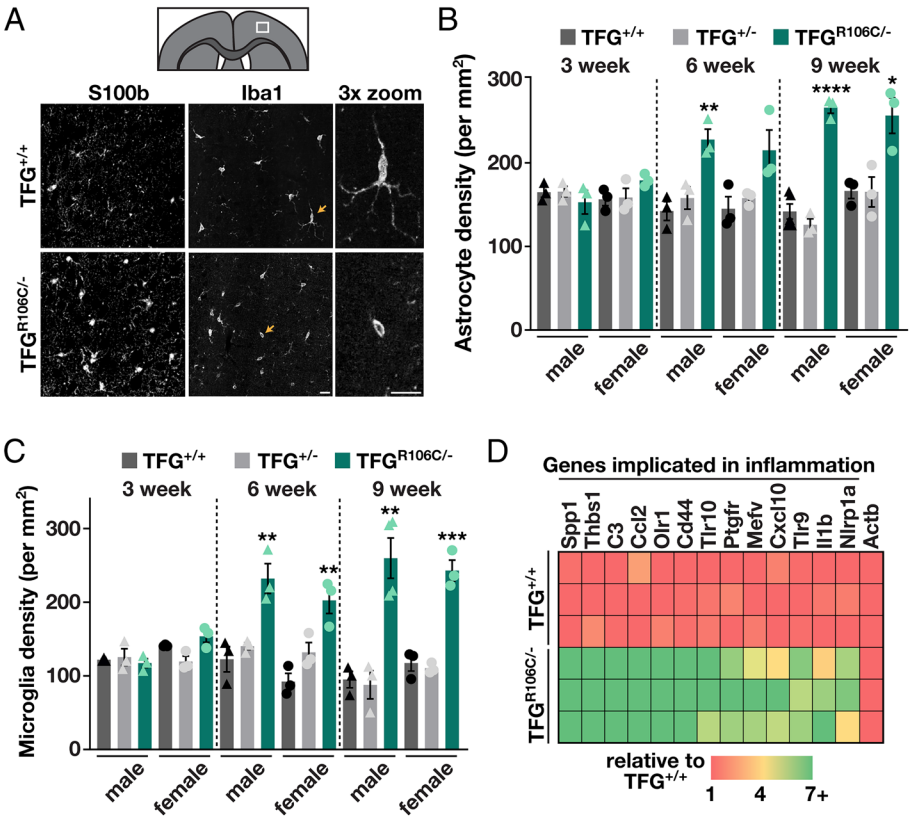

Fig. 3. TFG$^{R106C/-}$ animals exhibit progressive neuroinflammation. (*A*) Schematic (*Top*) and representative images (*Bottom*) of the cortical region analyzed using antibodies directed against S100b and Iba1 in 9-wk-old males. Orange arrows indicate examples of microglia, with zoomed images highlighting morphological changes in microglia between control and genome-edited animals (n = 5 each). (Scale bars, 20 mm.) (*B* and *C*) Quantification of the density of astrocytes (*B*) and microglia (*C*) in control and genome-edited animals over time (3 to 5 animals each; circles indicate females and triangles represent males). Error bars represent mean ± SEM. $^{**}P < 0.01$, $^{***}P < 0.001$, $^{****}P < 0.0001$, as calculated using ANOVA followed by a post hoc Tukey's multiple comparison tests, as compared to control (TFG$^{+/+}$). (*D*) Heat map highlighting highly up-regulated genes involved in inflammation in TFG$^{R106C/-}$ animals as compared to control (n = 3 biological replicates). Boxes represent values from individual animals.

body sway of TFG$^{R106C/-}$ males was more pronounced as compared to females at 6 wk of age (Fig. 2*B*), and by 9 wk of age, many TFG$^{R106C/-}$ males were dragging their hindlimbs, leading to diminished hind body sway relative to females (Fig. 2*B* and Movies S5 and S6). Additionally, decreased tail tip height was readily detectable in TFG$^{R106C/-}$ males at 6 wk of age and remained more pronounced several weeks later, as compared to TFG$^{R106C/-}$ females (Fig. 2*C*).

To define histological features that accompany loss of motor function in TFG$^{R106C/-}$ animals, we longitudinally examined global changes in brain architecture using LFB staining (*SI Appendix*, Fig. S1*C*). Strikingly, brains from 9-wk-old TFG$^{R106C/-}$ animals were dramatically smaller as compared to controls, exhibiting reduced cortical thickness and significantly enlarged ventricles (Fig. 2 *D*–*F* and *SI Appendix*, Fig. S1*D*). This finding paralleled the reduced body mass of TFG$^{R106C/-}$ animals, which were smaller in stature despite having full access to nutrients (*SI Appendix*, Fig. S1 *E* and *F*). Additionally, the area of the corpus callosum was significantly reduced in 6-wk and 9-wk-old TFG$^{R106C/-}$ animals relative to controls (Fig. 2*E*), similar to findings based on MRI of TFG-HSP patients as well as histological studies of rodents homozygous for the TFG p.R106C mutation at 25 wk of age (38, 43). In contrast, animals heterozygous for the TFG null allele (TFG±) exhibited no changes in motor function or brain morphology, even at 25 wk of age (*SI Appendix*, Fig. S2 *A*–*E*). Importantly, in 3-wk-old TFG$^{R106C/-}$ animals, brain morphology appeared largely normal (Fig. 2 *E* and *F*), suggesting that TFG-HSP is a neurodegenerative disease, as opposed to a neurodevelopmental disorder (35). Together, our data strongly suggest that the TFG$^{R106C/-}$ model represents an ideal platform for therapeutic drug discovery, with accelerated disease onset and progression relative to other rodent HSP models, while still retaining strong physiological relevance.

Neuroinflammation Accompanies Disease Progression in TFG$^{R106C/-}$ Animals. A signature feature of many neurodegenerative disorders is an increased presence of inflammatory markers throughout the brain, although few studies have focused specifically on HSP (44–50). We demonstrated previously that homozygous TFG p.R106C animals exhibit increased numbers of astrocytes and microglia in the motor cortex, albeit relatively late in disease with no elevation in reactive glia when gait deficits initially become apparent (43). To confirm whether neuroinflammation is similarly present in TFG$^{R106C/-}$ animals and determine its onset relative to gait dysfunction, we counted the number of astrocytes and microglia in the motor cortex over time (Fig. 3*A*). At 6 wk of age, the density of Iba1-positive microglia was increased significantly in mutant animals as compared to controls, and TFG$^{R106C/-}$ males additionally exhibited an elevated number of S100b-positive astrocytes. Within 3 additional wk, the density of both cell types was more pronounced and morphological changes in microglia (ramified to amoeboid) were observed in TFG$^{R106C/-}$ animals, consistent with their activation (Fig. 3 *A*–*C*).

To define molecular changes accompanying neuroinflammation, we conducted RNA sequencing using tissue from the primary motor region of 9-wk-old control animals and TFG$^{R106C/-}$ mutants. Gene ontology analysis revealed that expression of many genes involved in the inflammatory response was increased in TFG$^{R106C/-}$ animals

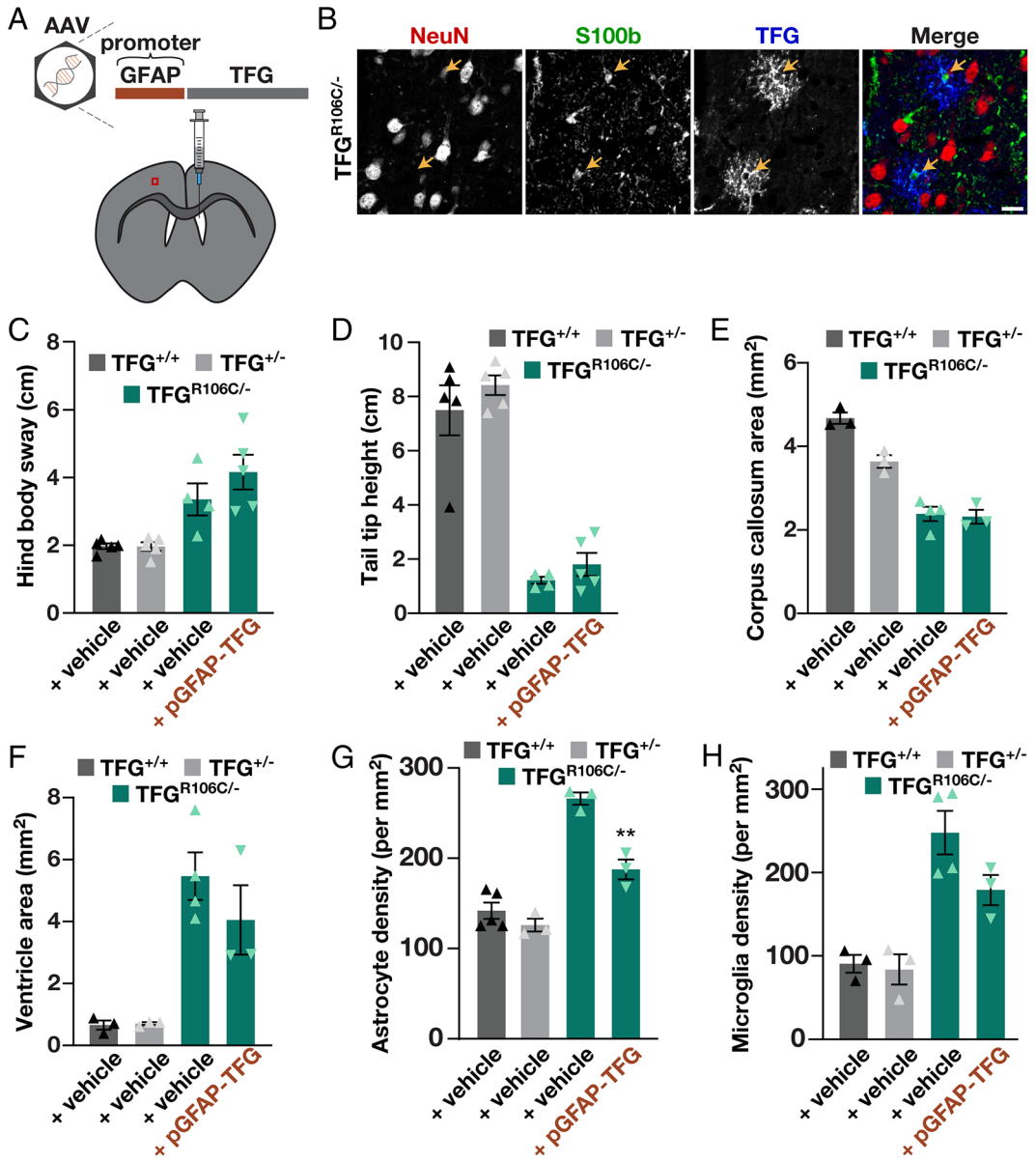

Fig. 4. Gene therapy targeting astrocytes modestly improves disease phenotypes exhibited by $TFG^{R106C/-}$ animals. (*A*) Schematic depicting gene therapy strategy in which an adeno-associated virus encoding TFG under control of the minimal GFAP promoter is delivered into the ventricles of $TFG^{R106C/-}$ pups. The boxed region indicates the approximate location of downstream imaging studies. (*B*) Representative images of tissue sections stained using antibodies directed against NeuN, S100b, and TFG (n = 3 biological replicates, minimally). Arrows highlight astrocytes expressing high levels of TFG. Bar, 20 mm. (*C* and *D*) Measurements of hind body sway (*C*) and tail tip height (*D*) of 9-wk-old males following neonatal ICV injections (4 to 5 each; triangles represent males). Error bars represent mean ± SEM. (*E* and *F*) Quantification of corpus callosum (*E*) and ventricle area (*F*) from LFB stained sections of 9-wk-old males following neonatal ICV injections (3 to 4 animals each; triangles represent males). Error bars represent mean ± SEM. (*G* and *H*) Quantification of astrocyte (*G*) and microglia (*H*) density in the motor cortex in 9-wk-old males following neonatal ICV injections (3 to 5 animals each; triangles represent males). Error bars represent mean ± SEM. $^{**}P < 0.01$, as calculated using *t* tests to compare $TFG^{R106C/-}$ animals treated with vehicle or a virus driving expression of TFG in astrocytes.

relative to control (Fig. 3*D* and *SI Appendix*, Fig. S3*A*), with only a small subset associated with this class exhibiting a modest decrease (*SI Appendix*, Fig. S3*B*). Additionally, genes typically expressed by activated astrocytes and microglia were up-regulated in mutant animals relative to controls (*SI Appendix*, Fig. S3 *C* and *D*) (51, 52). Taken together, these data demonstrate that pronounced neuroinflammation accompanies disease progression in $TFG^{R106C/-}$ animals.

Expression of WT TFG in Astrocytes Modestly Improves a Subset of $TFG^{R106C/-}$ Disease Phenotypes. Since astrogliosis accompanies disease progression in $TFG^{R106C/-}$ animals, we sought to understand whether reactive astrocytes are drivers of disease or whether they merely become activated as a downstream consequence of neuronal dysfunction. To address this question, we developed a therapeutic adeno-associated virus (AAV-PHP.eB) expressing WT TFG under the minimal GFAP promoter (GfaABC1D) to enable reexpression of TFG specifically in astrocytes that become reactive during the inflammatory process (53, 54). We administered the virus (or a vehicle control) via intracerebroventricular (ICV) injection to pups within 12 to 24 h of birth (Fig. 4*A*), a timepoint when the epithelial lining of the ventricles is not fully developed and the virus can permeate the surrounding parenchyma (55, 56). Animals were then examined 9 wk later, when disease phenotypes are normally severe. Based on immunohistochemistry, overall TFG levels were elevated in the motor cortex following virus delivery as compared to vehicle alone (Fig. 4*B* and *SI Appendix*, Fig. S4 *A* and *B*). In particular, increased TFG expression was detected in

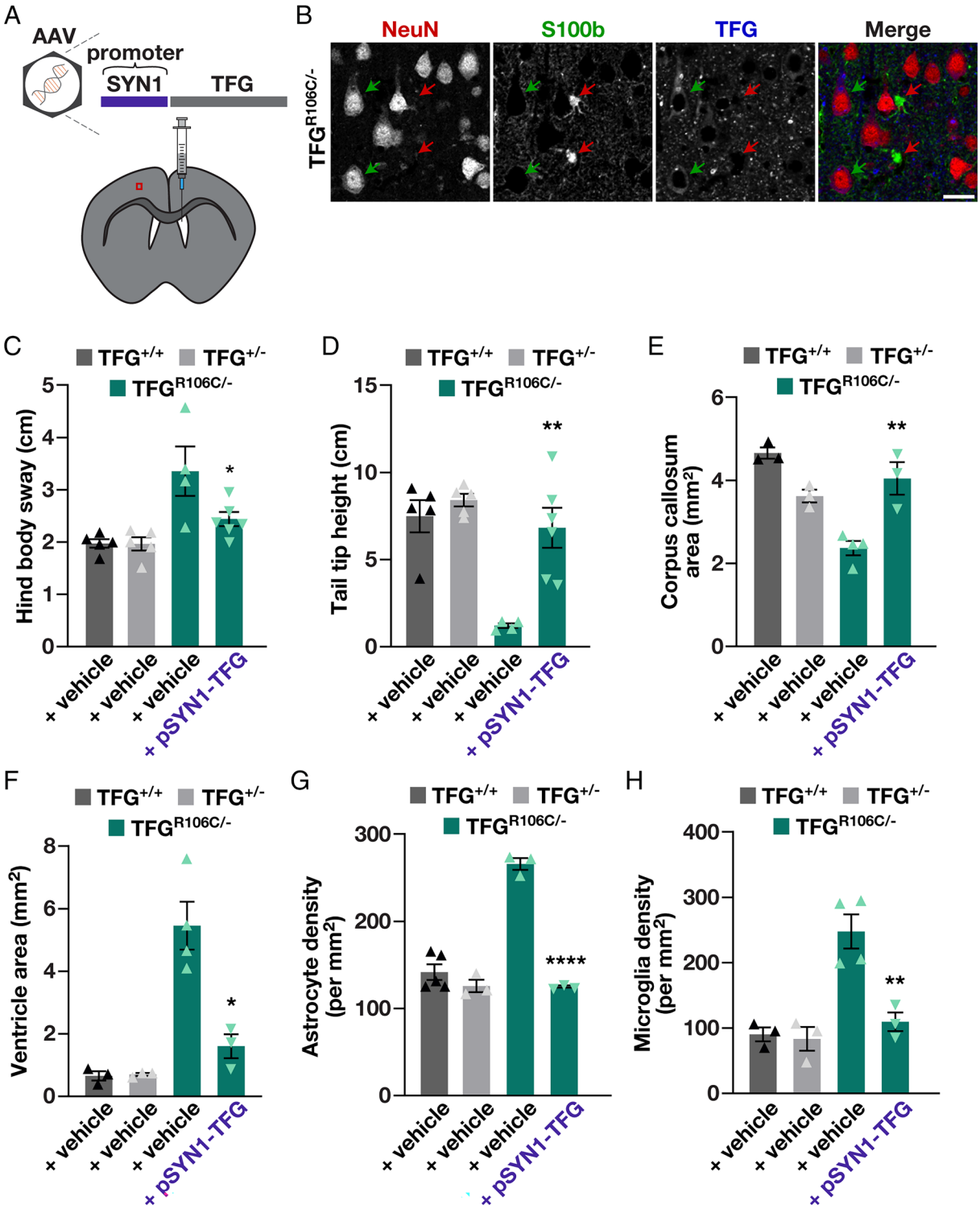

Fig. 5. Gene therapy targeting neurons rescues disease phenotypes exhibited by $TFG^{R106C/-}$ animals. (*A*) Schematic depicting gene therapy strategy in which an adeno-associated virus encoding TFG under control of the synapsin 1 (SYN1) promoter is delivered into the ventricles of $TFG^{R106C/-}$ pups. The boxed region indicates the approximate location of downstream imaging studies. (*B*) Representative images of tissue sections stained using antibodies directed against NeuN, S100b, and TFG (n = 3 biological replicates, minimally). Green arrows highlight neurons expressing elevated levels of TFG. Red arrows indicate astrocytes that lack increased TFG expression. (Scale bar, 20 μm.) (*C* and *D*) Measurements of hind body sway (*C*) and tail tip height (*D*) of 9-wk-old males following neonatal ICV injections (4 to 5 animal each; triangles represent males). Error bars represent mean ± SEM. $*P < 0.06$ and $**P < 0.01$, as calculated using *t* tests, comparing vehicle and a virus driving expression of TFG in neurons of $TFG^{R106C/-}$ animals. (*E* and *F*) Quantification of corpus callosum (*E*) and ventricle area (*F*) from LFB stained sections from 9-wk-old males following neonatal ICV injections (3 to 4 animals each; triangles represent males). Error bars represent mean ± SEM. $*P < 0.05$ and $**P < 0.01$, as calculated using *t* tests, comparing vehicle and a virus driving expression of TFG in neurons of $TFG^{R106C/-}$ animals (*G* and *H*) Quantification of astrocyte (*G*) and microglia (*H*) density in the motor cortex in males following neonatal ICV injections (3 to 5 animals each; triangles represent males). Error bars represent mean ± SEM. $**P < 0.01$, and $****P < 0.0001$, as calculated using *t* tests, comparing vehicle and a virus driving expression of TFG in neurons of $TFG^{R106C/-}$ animals.

approximately 16% of astrocytes and 6% of neurons, with few other cells showing evidence of being transduced (*SI Appendix*, Fig. S4*C*). Consistent with previous work, the minimal GFAP promoter failed to drive TFG expression within the cerebellum following AAV delivery (*SI Appendix*, Fig. S4*D*) (57).

We next determined whether WT TFG expression in GFAP-positive astrocytes ameliorated disease phenotypes in $TFG^{R106C/-}$ animals. Based on kinematic analysis, we found no statistically significant improvements in hind body sway, tail tip height, hip height, nor in the angle between the hip, knee, and ankle in virus-treated $TFG^{R106C/-}$ animals at 9 wk of age (Fig. 4 *C* and *D* and *SI Appendix*, Fig. S5 *A* and *B*). Similarly, astrocyte-specific TFG expression produced no statistically significant increase in body mass of $TFG^{R106C/-}$ animals (*SI Appendix*, Fig. S5*C*), nor improvements in their corpus callosum area, ventricle size, or cortical thickness (Fig. 4 *E* and *F* and *SI Appendix*, Fig. S5*D*). These data indicate that astrocyte-specific gene therapy is insufficient to significantly improve the motor function of $TFG^{R106C/-}$ animals.

However, qualitative assessment of $TFG^{R106C/-}$ animals treated with the astrocyte-specific virus suggested marginal improvement in gait (Movie S7). We therefore examined whether neuroinflammation may have been reduced when WT TFG was expressed in the astrocytes of $TFG^{R106C/-}$ animals, as compared to those receiving vehicle alone. Interestingly, we found a significant decrease in astrocyte density throughout the motor cortex of virus-treated $TFG^{R106C/-}$ animals, while microglia density remained elevated, more similar to vehicle-treated animals (Fig. 4 *G* and *H*). When taken together, these data suggest that a partial reduction of neuroinflammation has only a marginal impact on disease phenotypes associated with HSP.

Gene Therapy Targeting Neurons in $TFG^{R106C/-}$ Animals is Sufficient to Prevent Disease. Since reexpression of WT TFG in astrocytes failed to rescue gait deficits exhibited by $TFG^{R106C/-}$ animals, we next tested whether gene therapy targeting neurons would be sufficient to influence disease course. To test this idea, we developed a therapeutic AAV encoding TFG under the neuron-specific synapsin 1 (SYN1) promoter, and $TFG^{R106C/-}$ animals were subjected to treatment 12 to 24 h after birth (Fig. 5*A*). Similar to results using an astrocyte-specific virus, ICV injection of the neuron-specific virus provided long-lasting elevated expression of TFG in the targeted cell type, as compared to animals receiving vehicle alone (Fig. 5*B*). Additionally, TFG levels in the cerebellum were also increased under these conditions (*SI Appendix*, Fig. S4*E*). Strikingly, TFG expression in neurons was sufficient to rescue all disease phenotypes exhibited by $TFG^{R106C/-}$ animals, including gait deficits (Fig. 5 *C* and *D*, *SI Appendix*, Fig. S5 *A* and *B*, and Movie S7), anatomical brain changes (Fig. 5 *E* and *F* and *SI Appendix*, Fig. S5*D*), and body weight (*SI Appendix*, Fig. S5*C*).

Based on quantification of TFG expression in the motor cortex of injected animals, viral treatment targeting neurons provided an almost four-fold elevation in overall TFG expression (*SI Appendix*, Fig. S4 *A* and *B*), while expression in astrocytes simply restored TFG expression to approximately WT levels. To determine whether the high level of TFG expressed under synapsin 1 regulation was due to the promoter, we diluted the neuron-specific virus by approximately one-fifth of that used initially. To our surprise, injection of the diluted neuron-specific virus resulted in expression of TFG to nearly equivalent levels of the undiluted virus, suggesting that within the limited concentration range tested, sufficient virus was present to transduce all cells, and expression level was promoter-controlled (*SI Appendix*, Fig. S4 *A* and *B*).

As this therapeutic virus promoted WT TFG expression only in neurons, and the surrounding glial cells continued to produce only mutant TFG p.R106C, we questioned whether inflammation would remain elevated in virus-treated $TFG^{R106C/-}$ animals. Surprisingly, even though WT TFG expression was restricted to neurons, neuroinflammation was significantly reduced in treated $TFG^{R106C/-}$ animals (Fig. 5 *G* and *H*), suggesting that the inflammatory response is a consequence of neuronal degeneration, as opposed to a trigger that promotes decline in neuronal health.

Discussion

HSP has been estimated to affect ~1.8 out of 100,000 individuals worldwide, categorizing it as a rare disorder, although misdiagnosis may contribute to an underestimation of its prevalence (3). In general, the disease is considered to be monogenetic in nature, but nearly 100 different genes have been implicated in HSP pathology, which is characterized by axonopathy impacting neurons that comprise the CST leading to lower extremity bilateral spasticity and perturbed gait (58–60). Models to investigate the root causes of HSP are limited, contributing to slow progress in developing therapeutic options to curtail disease symptoms. Here, we used Sprague Dawley rats to establish a physiologically relevant HSP model, capitalizing on our previous work showing that rats homozygous for the TFG p.R106C mutation recapitulate several phenotypes observed in HSP patients, including progressive gait dysfunction, thinning of the corpus callosum, and axonopathy of the CST, with onset at ~4 mo of age (43). We now define an accelerated model of HSP, which we believe will serve as an even better platform to gauge the value of therapeutic interventions, given its rapid onset at 6 wk of age, followed by rapid disease progression.

Despite being expressed ubiquitously, pathological mutations in TFG result primarily in neurodegenerative disease, ranging from complicated forms of HSP, ALS, and Parkinson's disease to peripheral neuropathies, including Charcot–Marie–Tooth (CMT) disease and hereditary motor and sensory neuropathy with proximal dominancy (HMSN-P) (36–38, 61–73). However, loss of TFG function in tissues beyond the nervous system also causes defects in cellular function, likely due to impacts on membrane trafficking pathways in which TFG has been implicated (39–41). For example, in pancreatic beta cells, depletion of TFG blocks cell proliferation and significantly impairs glucose-induced insulin secretion (74). Nonetheless, HSP patients harboring TFG point mutations present mainly with neurological symptoms, suggesting that neurons are more sensitive to disrupted TFG function than other cell types (36–38, 61–73). Consistent with this idea, gene therapy to drive neuron-specific TFG expression was sufficient to rescue all phenotypes identified in $TFG^{R106C/-}$ animals. Surprisingly, the resulting high levels of TFG in neurons were well tolerated, contrasting previous work suggesting that TFG overexpression is toxic due to the titration of secretory pathway components away from their sites of action (40). Under these conditions, overexpressed TFG exhibits a propensity to assemble into enlarged condensates, which retain interacting partners, including the COPII component Sec23 (40). Further studies will be necessary to determine whether persistently high levels of TFG in vivo lead to the formation of fibrils, which have been suggested to arise in patients expressing dominant-acting TFG mutations (p.G269V and p.P285L) that underlie CMT and HMSN-P (75). If so, gene therapy strategies will need to leverage weaker promoters to facilitate the expression of lower levels of TFG in those with recessive TFG mutations.

Although expression of TFG in astrocytes failed to fully remediate phenotypes shown by $TFG^{R106C/-}$ animals, qualitative improvements in gait were evident, as compared to animals treated with vehicle alone. These data suggest that TFG contributes positively to the function of neuroglia, potentially enhancing the secretion of trophic factors that support neuronal maintenance, including components of the extracellular matrix (76–78). However, despite an enhanced microenvironment, mutant $TFG^{R106C/-}$ neurons continue to degenerate under these conditions, and animals lose the ability to walk normally, likely due to a cell-autonomous defect in secretory and/or endocytic cargo trafficking (42, 43). Striking, gene therapy-mediated rescue of neurons in $TFG^{R106C/-}$ animals not only prevented neurodegeneration but also blocked activation of the inflammatory response throughout the motor cortex. These findings highlight the active communication system that exists between neurons and neuroglia within the motor cortex and suggest that cell-autonomous neuronal degeneration in HSP could result in the release of signals that trigger neuroinflammation, which can ultimately become detrimental to neuronal health (29, 79, 80). Notably, in $TFG^{R106C/-}$ animals, the neuroprotective chemokine fractalkine/CX3CL1 expressed by neurons is down-regulated, which is predicted to promote the expression of proinflammatory genes in activated microglia (81, 82). Modulation of fractalkine signaling may thus be a therapeutic avenue to consider in the context of HSP. Consistent with this idea, enhanced fractalkine signaling appears to be neuroprotective in models of both Alzheimer's and Parkinson's disease (83, 84).

Overall, our results indicate that targeted gene therapy may be a beneficial approach to treating HSP subtypes. Gene therapy for the devastating MNDs spinal muscular atrophy is already saving lives (85, 86). Moreover, preclinical studies leveraging viral expression of some HSP-associated genes have already shown safety in rodents and nonhuman primates, as well as disease stabilization in a human clinical trial (87, 88). With improved models now available for HSP, we anticipate an acceleration in the development of therapeutic options for the disease, which should support the launching of clinical trials in the near future.

Materials and Methods

Generation and Husbandry of CRISPR/Cas9-Edited Sprague Dawley Rats. All animal studies were approved by the Institutional Animal Care and Use Committee of the University of Wisconsin-Madison. Animals were maintained in Innovive cages (12-h light/12-h dark cycle) with free access to food and water. Animals were not singly housed, and health checks were performed for all animals daily. University and facility guidelines were adhered to for anesthesia and euthanasia under the Pain, Distress, or Death as Experimental End-Points and Euthanasia Policy from the School of Medicine and Public Health Animal Care and Use Committee.

CRISPR/Cas9-mediated genome editing of Sprague Dawley embryos was performed as described previously using a guide RNA directed at exon 4 of TFG (5′-GTCGAGAACTGATAGAACTT-3′) to generate a deletion allele (43). Edited animals were outcrossed with WT Sprague Dawley rats (Envigo).

Animals were assigned to experimental groups based on genotype and gender. The number of animals in each study is indicated within figures and associated figure legends. Experimenters were blinded to animal genotype, when possible. All experiments were performed during the 12-h light cycle.

Protein Expression Analysis by Immunoblot. Following euthanization by CO_2 asphyxiation, brain tissue was quickly harvested and drop frozen in liquid nitrogen in accordance with the Pain, Distress, or Death as Experimental End-Points and Euthanasia Policy from the School of Medicine and Public Health Animal Care and Use Committee. Tissues were ground in liquid nitrogen and resuspended in SDS sample buffer. Tissues were further lysed by bead beating, and trituration through a small gauge needle. Lysed samples were separated by sodium dodecyl sulfate-polyacrylamide gel electrophoresis and transferred to polyvinylidene fluoride membranes. After blocking, proteins of interest were detected using primary antibodies directed against TFG (NBP2-62212, Novus) or b-actin (A1978, Sigma), secondary antibodies (HRP-linked anti-mouse IgG; 31430, Thermo), and developed using SuperSignal West Femto Maximum Sensitivity Substrate (PI34095, Thermo). Band intensities were normalized to loading controls and then compared to control animals.

Mass Spectrometry. The following materials were used for mass spectrometry analysis: Acetonitrile (A955-4, Optima LC–MS), Methanol (A454SK-4, Optima LC/MS Grade, Fisher Chemical), tris(2-carboxyethyl)phosphine (C4706, Sigma-Aldrich), Chloroacetamide (C0267, Sigma-Aldrich), Formic acid (FA) (PI28905, Thermo Scientific), Guanidine HCl (G4505, Sigma-Aldrich), Urea (U-5378, Sigma-Aldrich), Lysyl EndopeptidaseR (LysC)-10 Au (100369-826 (EA), VWR), Trypsin (Promega, V5113). For proteomic analysis, a 75 to 360 μm inner-outer diameter bare-fused silica capillary was packed with 1.7 μm diameter, 130 Å pore size, Bridged Ethylene Hybrid C18 particles (Waters) to a final length of ~40 cm. Brain powder produced following grinding in liquid nitrogen was suspended in 6 M Guanidine HCl. Probe sonication was carried out to disrupt the tissue thoroughly at 4°C. Afterward, proteins were precipitated with methanol at the volume ratio of 1:9 (guanidine solution:methanol, v:v), and centrifuged at 9,000×*g* for 5 min. Supernatant was aspirated and the protein pellets sat for 10 min at room temperature to dry remaining liquid in the bottom of the tube. 400 μL lysis buffer [8 M urea with 100 mM tris(2-carboxyethyl) phosphine, 40 mM chloroacetamide, and 100 mM tris (pH = 8.0)] was added to each sample and vortexed until the protein pellets were fully dissolved. LysC was added to each sample with a protein:enzyme ratio 50:1, and digestion was performed for 4.5 h at room temperature. Trypsin at 50:1 protein:enzyme was added to each sample after diluting the lysis buffer to 2 M urea, and further digestion was carried out overnight at room temperature. Desalting was carried out to remove excess salts, starting with equilibration of desalting columns with 100% acetonitrile (ACN), followed by 0.2% formic acid (FA) wash to remove ACN in the column. The acidified peptide mixture was loaded onto the desalting column, followed by 0.2% FA wash. Peptides were eluted with 80% ACN with 0.2% FA, and vacuum dried for storage at −80°C. Resuspension was carried out with 0.2% FA, after which peptide concentration was measured using a quantitative colorimetric peptide assay.

Off-line high pH fractionation of peptides was carried out on an Agilent 1260 Infinity Binary LC system. Fractionation mobile phase A was 10 mM ammonium formate, and mobile phase B was 80% methanol with 10 mM ammonium formate. Both mobile phases were of pH 10 adjusted by ammonium hydroxide. 16 fractions were collected for each sample and were combined into four mixed fractions. The combined fractions then were separated online with the following LC setups: mobile phase A was water with 0.2% formic acid (FA) and B was 70% ACN with 0.2% FA. Peptides were loaded onto the column for 10 min at 0.40 μL/min. Mobile phase B increased from 0 to 5% in 10 min, then to 55% B at 75 min, 100% B at 76 min and held for 3 min at 100% B, decreased to 0% B at 80 min, and a 10 min re-equilibration at 0% B. For each analysis, 2.0 μg peptides were injected using an autosampler. Survey scans of precursors were taken from 300 to 1,350 m/z at 240 K resolving power. Maximum injection time was 50 ms, and the automatic gain control (AGC) target was 1.5E6. Tandem MS was performed using an isolation window of 0.7 Th with a dynamic exclusion time of 20 s. Selected precursors were fragmented using a normalized collision energy level of 25%. MS2 AGC target was 3E4 with a maximum injection time of 11 ms. Scan range was 200 to 1,200 m/z. Scans were taken at the Turbo speed, and only peptides with a charge state of +2 or greater were selected for fragmentation.

LC–MS files for proteomics were searched in Maxquant (version 1.5.2.8). Original outputs from Maxquant were inspected and potential contaminant proteins, protein groups that contain proteins identified with decoy peptide sequence, and those identified only with modification site were removed. Label-free quantification intensities were used as the quantification metric.

RNA Sequencing. Animals were euthanized by CO_2 asphyxiation, and brain tissue was quickly harvested in accordance with the Pain, Distress, or Death as Experimental End-Points and Euthanasia Policy from the School of Medicine and Public Health Animal Care and Use Committee. The region containing the motor

cortex was quickly dissected on ice, placed into trizol, and flash frozen in liquid nitrogen. RNA was isolated using phenol–chloroform extraction, followed by two successive precipitation steps in isopropanol/2M sodium chloride, followed by lithium chloride. The lithium chloride pellet was washed with 70% ethanol and resuspended in nuclease-free water. RNA sequencing of samples of sufficient quality was performed by Novogene. The Database for Annotation, Visualization and Integrated Discovery was used to identify genes involved in inflammation (89, 90).

Quantitative Gait Measurements. Animals were evaluated as described previously (43). Briefly, animals marked with points of interest were recorded as they traversed a flat platform. Videos were assessed to ensure only uninterrupted forward motion was included. Points of interest were assigned using a neural network trained to track specific anatomical features. Custom MATLAB scripts were used to calculate kinematic parameters. Data from two recording days were averaged.

Quantification of Brain Region Size, Cell Density, and TFG Expression. For preservation of brain tissue, animals were deeply anesthetized using isoflurane and transcardially perfused with PBS, followed by 4% PFA. Five-micron coronal sections of paraffin-embedded tissue were prepared using a microtome and captured onto glass slides. For size measurements, deparaffinized sections were stained with LFB to mark myelinated axons in the corpus callosum and counterstained with hematoxylin and eosin or cresyl violet. Images were acquired using a uScope HXII slide scanner and analyzed by tracing the corpus callosum or ventricles with the polygon tool in ImageJ. The area of each ventricle was summed to give the total area. For cortical thickness measurements, a line was anchored just above the corpus callosum in the primary motor cortex and the shortest line to the exterior of the cortex was drawn. This was repeated five times in each hemisphere and averaged to yield the final cortical thickness measurement.

For immunofluorescence studies, heat-induced epitope retrieval of deparaffinized sections was performed at high temperature in pH 6 buffer. After blocking with 10% donkey serum, sections were incubated with primary antibodies overnight, washed, and incubated with dye-labeled secondary antibodies prior to mounting with Vectashield mounting medium. Primary antibodies used were TFG (NBP2-62212, Novus), Iba1 (019-19741, FUJIFILM Wako Pure Chemical Corporation), S100b (GA50461-2, Agilent), NeuN (MAB377, Sigma), and Calbindin (13176, Cell Signaling). For quantification of cell density, images encompassing the cortex and corpus callosum were acquired with a Nikon Eclipse Ti2-E spinning disk confocal microscope equipped with a Yokogawa CSU-W1 scanhead and an ORCA-Fusion BT sCMOS camera at 20× magnification. The number of astrocytes and microglia were quantified in a 0.23 mm^2 rectangle centered over the motor cortex using Imaris software.

For quantification of TFG expression, additional 60× images were captured in the primary motor cortex, centered at the midpoint between layers 2/3 (identified by the trajectory of layer 4 in the primary somatosensory region) and the top of the corpus callosum. Square regions of interest were captured (z-series of 15 × 0.5 mm sections), and background subtracted intensities of sum intensity projections were calculated for each hemisphere and averaged. The percentage of cells transduced with the GFAP-driven virus was quantified by calculating the number of NeuN-positive neurons, S100b-positive astrocytes, or DAPI-positive cells that failed to immunostain positively for either S100b and NeuN, which expressed TFG above background and dividing by the total number of each cell type in a region of interest.

AAV Production and Injection. Full-length *Rattus norvegicus* TFG (synthesized by General Biosystems), together with either the SYN1 or minimal GFAP promoter (gfaABC1D, kind gifts from Jeffery A. Johnson, University of Wisconsin-Madison) were cloned into the pAAV backbone (37825, Addgene) and sequences were verified. Purified AAV in the PHP.eB capsid was generated by Vigene (Charles River). Viruses were brought to 1.2×10^{13} genome copies per mL with PBS and trypan blue (0.05%), and 5 μL was injected into each ventricle (2 mm lateral to bregma, 1 mm deep) in isoflurane-anesthetized pups within 12 to 24 h after birth. Mock injections (vehicle alone) contained 0.05% trypan blue in PBS.

Statistical Methods. All *P* values were determined using unpaired *t* tests or an ANOVA (followed by a Tukey post hoc test), calculated using GraphPad Prism. All data are shown as mean ± SEM, unless otherwise noted. In nearly all cases, significant differences are indicated by a *P* value less than 0.05. No data were excluded, and sample size was determined based on prior work (43).

Data, Materials, and Software Availability. All study data are included in the article and/or supporting information.

ACKNOWLEDGMENTS. This work was supported in part by NIH Grants R01 NS124165 (to A.A.), R35 GM134865 (to A.A.), T32 GM141013 (to C.A.M.), P41 GM108538 (to J.J.C.), and R35 GM118110 (to J.J.C.); the University of Wisconsin Carbone Cancer Center (UWCCC) Grant P30 CA014520; the Waisman Center Core Grant P50 HD105353. Support was also provided by the UWCCC Genome Editing and Animal Models Shared Resource, the UWCCC Flow Cytometry Laboratory, and the UW Optical Imaging Core facility. We thank members of the Audhya lab for critically reading this manuscript.

Author affiliations: [a]Department of Biomolecular Chemistry, University of Wisconsin School of Medicine and Public Health, Madison, WI 53705; [b]Department of Chemistry, University of Wisconsin, Madison, WI 53706; [c]National Center for Quantitative Biology of Complex Systems, University of Wisconsin, Madison, WI 53706; and [d]Morgridge Institute for Research, Madison, WI 53715

1. R. Chaudhary, V. Agarwal, M. Rehman, A. S. Kaushik, V. Mishra, Genetic architecture of motor neuron diseases. *J. Neurol. Sci.* **434**, 120099 (2022).
2. L. A. Foster, M. K. Salajegheh, Motor neuron disease: Pathophysiology, diagnosis, and management. *Am. J. Med.* **132**, 32–37 (2019).
3. C. Blackstone, Converging cellular themes for the hereditary spastic paraplegias. *Curr. Opin. Neurobiol.* **51**, 139–146 (2018).
4. T. Fullam, J. Statland, Upper motor neuron disorders: Primary lateral sclerosis, upper motor neuron dominant amyotrophic lateral sclerosis, and hereditary spastic paraplegia. *Brain Sci.* **11**, 611 (2021).
5. J. P. Taylor, R. H. Brown, D. W. Cleveland, Decoding ALS: From genes to mechanism. *Nature* **539**, 197–206 (2016).
6. R. Mejzini *et al.*, ALS Genetics, mechanisms, and therapeutics: Where are we now?. *Front Neurosci.* **13**, 1310 (2019).
7. M. K. Floeter *et al.*, Clinical care and therapeutic trials in PLS. *Amyotrophic Lateral Scler. Frontotemporal Degener.* **21**, 67–73 (2020).
8. B. Sever *et al.*, Comprehensive research on past and future therapeutic strategies devoted to treatment of amyotrophic lateral sclerosis. *Int. J. Mol. Sci.* **23**, 2400 (2022).
9. M. Bellofatto, G. De Michele, A. Iovino, A. Filla, Management of hereditary spastic paraplegia: A systematic review of the literature. *Front. Neurol.* **10**, 3 (2019).
10. B. Trummer, D. Haubenberger, C. Blackstone, C. Blackstone, Clinical trial designs and measures in hereditary spastic paraplegias. *Front. Neurol.* **9**, 1017 (2018).
11. C. S. Tseng, Y. W. Chao, Y. H. Liu, Y. S. Huang, H. W. Chao, Dysregulated proteostasis network in neuronal diseases. *Front. Cell Dev. Biol.* **11**, 1075215 (2023).
12. G. Cenini, A. Lloret, R. Cascella, Oxidative stress in neurodegenerative diseases: From a mitochondrial point of view. *Oxid. Med. Cell Longev.* **2019**, 2105607 (2019).
13. M. Kodavati, H. Wang, M. L. Hegde, Altered mitochondrial dynamics in motor neuron disease: An emerging perspective. *Cells* **9**, 1065 (2020).
14. M. Nagai *et al.*, Astrocytes expressing ALS-linked mutated SOD1 release factors selectively toxic to motor neurons. *Nat. Neurosci.* **10**, 615–622 (2007).
15. K. Qian *et al.*, Sporadic ALS astrocytes induce neuronal degeneration in vivo. *Stem Cell Rep.* **8**, 843–855 (2017).
16. A. Kia, K. McAvoy, K. Krishnamurthy, D. Trotti, P. Pasinelli, Astrocytes expressing ALS-linked mutant FUS induce motor neuron death through release of tumor necrosis factor-alpha. *Glia* **66**, 1016–1033 (2018).
17. A. M. Haidet-Phillips *et al.*, Astrocytes from familial and sporadic ALS patients are toxic to motor neurons. *Nat. Biotechnol.* **29**, 824–828 (2011).
18. J. M. Edgar *et al.*, Oligodendroglial modulation of fast axonal transport in a mouse model of hereditary spastic paraplegia. *J. Cell Biol.* **166**, 121–131 (2004).
19. K. A. Luders, J. Patzig, M. Simons, K.-A. Nave, H. B. Werner, Genetic dissection of oligodendroglial and neuronal Plp1 function in a novel mouse model of spastic paraplegia type 2. *Glia* **65**, 1762–1776 (2017).
20. Y. Mou *et al.*, Impaired lipid metabolism in astrocytes underlies degeneration of cortical projection neurons in hereditary spastic paraplegia. *Acta Neuropathol. Commun.* **8**, 214 (2020).
21. H. S. Kwon, S. H. Koh, Neuroinflammation in neurodegenerative disorders: The roles of microglia and astrocytes. *Transl. Neurodegener.* **9**, 42 (2020).
22. S. A. Johnson *et al.*, Paganoni, pharmacotherapy for amyotrophic lateral sclerosis: A Review of approved and upcoming agents. *Drugs* **82**, 1367–1388 (2022).
23. F. De Marchi *et al.*, Interplay between immunity and amyotrophic lateral sclerosis: Clinical impact. *Neurosci. Biobehav. Rev.* **127**, 958–978 (2021).
24. M. Wosiski-Kuhn, M. S. Lyon, J. Caress, C. Milligan, Inflammation, immunity, and amyotrophic lateral sclerosis: II. Immune-modulating therapies. *Muscle Nerve* **59**, 23–33 (2019).
25. J. Groh, M. Hörner, R. Martini, Teriflunomide attenuates neuroinflammation-related neural damage in mice carrying human PLP1 mutations. *J. Neuroinflammation* **15**, 194 (2018).

26. M. Hörner *et al.*, CNS-associated T-lymphocytes in a mouse model of Hereditary Spastic Paraplegia type 11 (SPG11) are therapeutic targets for established immunomodulators. *Exp. Neurol.* **355**, 114119 (2022).
27. L. Krumm *et al.*, Neuroinflammatory disease signatures in SPG11-related hereditary spastic paraplegia patients. *Acta Neuropathol.* **147**, 28 (2024).
28. D. J. DiSabato, N. Quan, J. P. Godbout, Neuroinflammation: The devil is in the details. *J. Neurochem.* **139**, 136–153 (2016).
29. P. Varghaei *et al.*, Genetic, structural and clinical analysis of spastic paraplegia 4. *Parkinsonism Relat. Disord.* **98**, 62–69 (2022).
30. L. Parodi, G. Coarelli, G. Stevanin, A. Brice, A. Durr, Hereditary ataxias and paraparesias: Clinical and genetic update. *Curr. Opin. Neurol.* **31**, 462–471 (2018).
31. J. M. Statland *et al.*, Primary lateral sclerosis. *Neurol. Clin.* **33**, 749–760 (2015).
32. C. Quinn, L. Elman, Amyotrophic lateral sclerosis and other motor neuron diseases. *Continuum* **26**, 1323–1347 (2020).
33. L. Van de Vondel *et al.*, De novo and dominantly inherited SPTAN1 mutations cause spastic paraplegia and cerebellar ataxia. *Mov. Disord.* **37**, 1175–1186 (2022).
34. H. Morsy *et al.*, Expanding SPTAN1 monoallelic variant associated disorders: From epileptic encephalopathy to pure spastic paraplegia and ataxia. *Genet. Med.* **25**, 76–89 (2023).
35. L. E. O. Elsayed, I. Z. Eltazi, A. E. Ahmed, G. Stevanin, Insights into clinical, genetic, and pathological aspects of hereditary spastic paraplegias: A comprehensive overview. *Front. Mol. Biosci.* **8**, 690899 (2021).
36. C. Beetz *et al.*, Inhibition of TFG function causes hereditary axon degeneration by impairing endoplasmic reticulum structure. *Proc. Natl. Acad. Sci. U.S.A.* **110**, 5091–5096 (2013).
37. G. V. Harlalka *et al.*, Novel genetic, clinical, and pathomechanistic insights into TFG-associated hereditary spastic paraplegia. *Hum. Mutat.* **37**, 1157–1161 (2016).
38. A. Catania *et al.*, R106C TFG variant causes infantile neuroaxonal dystrophy "plus" syndrome. *Neurogenetics* **19**, 179–187 (2018).
39. K. Witte *et al.*, TFG-1 function in protein secretion and oncogenesis. *Nat. Cell Biol.* **13**, 550–558 (2011).
40. A. Johnson *et al.*, TFG clusters COPII-coated transport carriers and promotes early secretory pathway organization. *EMBO J.* **34**, 811–827 (2015).
41. M. G. Hanna *et al.*, TFG facilitates outer coat disassembly on COPII transport carriers to promote tethering and fusion with ER–Golgi intermediate compartments. *Proc. Natl. Acad. Sci. U.S.A.* **114**, E7707–E7716 (2017).
42. E. L. Slosarek *et al.*, Pathogenic TFG mutations underlying hereditary spastic paraplegia impair secretory protein trafficking and axon fasciculation. *Cell Rep.* **24**, 2248–2260 (2018).
43. J. L. Peotter *et al.*, TFG regulates secretory and endosomal sorting pathways in neurons to promote their activity and maintenance. *Proc. Natl. Acad. Sci. U.S.A.* **119**, e2210649119 (2022).
44. J. H. Lim *et al.*, ARL6IP1 gene delivery reduces neuroinflammation and neurodegenerative pathology in hereditary spastic paraplegia model. *J. Exp. Med.* **221**, e20230367 (2024).
45. A. Adamu, S. Li, F. Gao, G. Xue, The role of neuroinflammation in neurodegenerative diseases: Current understanding and future therapeutic targets. *Front. Aging Neurosci.* **16**, 1347987 (2024).
46. G. Morello, A. G. Spampinato, S. Cavallaro, Neuroinflammation and ALS: Transcriptomic insights into molecular disease mechanisms and therapeutic targets. *Mediators Inflammation* **2017**, 7070469 (2017).
47. S. Paganoni *et al.*, Imaging of glia activation in people with primary lateral sclerosis. *Neuroimage Clin.* **17**, 347–353 (2018).
48. M. E. McCauley, R. H. Baloh, Inflammation in ALS/FTD pathogenesis. *Acta Neuropathol.* **137**, 715–730 (2019).
49. K. Qian *et al.*, Revisiting the critical roles of reactive astrocytes in neurodegeneration. *Mol. Psychiatry* **28**, 2697–2706 (2023).
50. B. A. Ashford *et al.*, Review: Microglia in motor neuron disease. *Neuropathol. Appl. Neurobiol.* **47**, 179–197 (2021).
51. C. Escartin *et al.*, Reactive astrocyte nomenclature, definitions, and future directions. *Nat. Neurosci.* **24**, 312–325 (2021).
52. A. M. Jurga, M. Paleczna, K. Z. Kuter, Overview of general and discriminating markers of differential microglia phenotypes. *Front. Cell Neurosci.* **14**, 198 (2020).
53. Y. Lee, A. Messing, M. Su, M. Brenner, GFAP promoter elements required for region-specific and astrocyte-specific expression. *Glia* **56**, 481–493 (2008).
54. K. Chan *et al.*, Engineered AAVs for efficient noninvasive gene delivery to the central and peripheral nervous systems. *Nat. Neurosci.* **20**, 1172–1179 (2017).
55. M. A. Passini, J. H. Wolfe, Widespread gene delivery and structure-specific patterns of expression in the brain after intraventricular injections of neonatal mice with an adeno-associated virus vector. *J. Virol.* **75**, 12382–12392 (2001).
56. J.-Y. Kim, S. D. Grunke, Y. Levites, T. E. Golde, J. L. Jankowsky, Intracerebroventricular viral injection of the neonatal mouse brain for persistent and widespread neuronal transduction. *J. Vis. Exp.* **15**, 51863 (2014).
57. A. Sanchez *et al.*, Cerebellar astrocyte transduction as gene therapy for megalencephalic leukoencephalopathy. *Neurotherapeutics* **17**, 2041–2053 (2020).
58. E. Panza, A. Meyyazhagan, A. Orlacchio, Hereditary spastic paraplegia: Genetic heterogeneity and common pathways. *Exp. Neurol.* **357**, 114203 (2022).
59. M. Boutry, S. Morais, G. Stevanin, Update on the genetics of spastic paraplegias. *Curr. Neurol. Neurosci. Rep.* **19**, 18 (2019).
60. W. A. Awuah *et al.*, Hereditary spastic paraplegia: Novel insights into the pathogenesis and management. *SAGE Open Med.* **12**, 20503121231221941 (2024).
61. M. A. Kilic *et al.*, A retrospective review of 18 patients with childhood-onset hereditary spastic paraplegia nine with novel variants. *Pediatr. Neurol.* **152**, 189–195 (2024).
62. L. E. O. Elsayed *et al.*, Hereditary spastic paraplegias: Identification of a novel SPG57 variant affecting TFG oligomerization and description of HSP subtypes in Sudan. *Eur. J. Hum. Genet.* **25**, 100–110 (2016).
63. M. Khorrami *et al.*, Homozygous TFG gene variants expanding the mutational and clinical spectrum of hereditary spastic paraplegia 57 and a review of literature. *J. Hum. Genet.* **66**, 973–981 (2021).
64. P.-C. Tsai *et al.*, A novel TFG mutation causes Charcot-Marie-Tooth disease type 2 and impairs TFG function. *Neurology* **83**, 903–912 (2014).
65. Y. Cao *et al.*, Clinical and genetic spectrum in a large cohort of hereditary spastic paraplegia. *Mov. Disord.* **39**, 651–662 (2024).
66. L. Xu *et al.*, Novel TFG mutation causes autosomal-dominant spastic paraplegia and defects in autophagy. *J. Med. Genet.* **2023**, 109485 (2023).
67. D. Yoo *et al.*, A novel TFG mutation in a Korean family with α-synucleinopathy and amyotrophic lateral sclerosis. *Mov. Disord.* **37**, 384–391 (2022).
68. T. Miyabayashi *et al.*, A novel homozygous mutation of the TFG gene in a patient with early onset spastic paraplegia and later onset sensorimotor polyneuropathy. *J. Hum. Genet.* **64**, 171–176 (2019).
69. H. Tariq, S. Naz, TFG associated hereditary spastic paraplegia: An addition to the phenotypic spectrum. *Neurogenetics* **18**, 105–109 (2017).
70. M. Khani, H. Shamshiri, A. Alavi, S. Na, E. Elahi, Identification of novel TFG mutation in HMSN-P pedigree: Emphasis on variable clinical presentations. *J. Neurol. Sci.* **369**, 318–323 (2016).
71. A. Alavi *et al.*, HMSN-P caused by p.Pro285Leu mutation in TFG is not confined to patients with Far East ancestry. *Neurobiol. Aging* **36**, 1–7 (2015).
72. S. S. Lee *et al.*, Proximal dominant hereditary motor and sensory neuropathy with proximal dominance association with mutation in the TRK-fused gene. *JAMA Neurol.* **70**, 607–615 (2013).
73. H. Ishiura *et al.*, The TRK-fused gene is mutated in hereditary motor and sensory neuropathy with proximal dominant involvement. *Am. J. Hum. Genet.* **91**, 320–329 (2012).
74. T. Yamamotoya *et al.*, Trk-fused gene (TFG) regulates pancreatic β cell mass and insulin secretory activity. *Sci. Rep.* **7**, 13026 (2017).
75. G. M. Rosenberg *et al.*, Bioinformatic identification of previously unrecognized amyloidogenic proteins. *J. Biol. Chem.* **298**, 101920 (2022).
76. R. A. Chiareli *et al.*, The Role of astrocytes in the neurorepair process. *Front. Cell Dev. Biol.* **9**, 665795 (2021).
77. L. Vargova, E. Sykova, Astrocytes and extracellular matrix in extrasynaptic volume transmission. *Philos. Trans. R. Soc. Lond. B, Biol. Sci.* **369**, 20130608 (2014).
78. S. Wiese, M. Karus, A. Faissner, Astrocytes as a source for extracellular matrix molecules and cytokines. *Front. Pharmacol.* **3**, 120 (2012).
79. Z. Szepesi, O. Manouchehrian, S. Bachiller, T. Deierborg, Bidirectional microglia-neuron communication in health and disease. *Front. Cell Neurosci.* **12**, 323 (2018).
80. S. Mederos, C. González-Arias, G. Perea, Astrocyte-neuron networks: A multilane highway of signaling for homeostatic brain function. *Front. Synaptic Neurosci.* **10**, 45 (2018).
81. N. P. Camacho-Hernández, F. Peña-Ortega, Fractalkine/CX3CR1-dependent modulation of synaptic and network plasticity in health and disease. *Neural Plast.* **2023**, 4637073 (2023).
82. P. Luo, S. Feng Chu, Z. Zhang, C. Yuan Xia, N. Hong Chen, Fractalkine/CX3CR1 is involved in the cross-talk between neuron and glia in neurological diseases. *Brain Res. Bull.* **146**, 12–21 (2019).
83. E. Angelopoulou, Y. N. Paudel, M. F. Shaikh, C. Piperi, Fractalkine (CX3CL1) signaling and neuroinflammation in Parkinson's disease: Potential clinical and therapeutic implications. *Pharmacol. Res.* **158**, 104930 (2020).
84. G. Bivona, M. Iemmolo, G. Ghersi, CX3CL1 Pathway as a molecular target for treatment strategies in Alzheimer's Disease. *Int. J. Mol. Sci.* **24**, 8230 (2023).
85. J. R. Mendell *et al.*, Single-dose gene-replacement therapy for spinal muscular atrophy. *N. Engl. J. Med.* **377**, 1713–1722 (2017).
86. S. A. Al-Zaidy *et al.*, AVXS-101 (Onasemnogene Abeparvovec) for SMA1: Comparative study with a prospective natural history cohort. *J. Neuromuscul. Dis.* **6**, 307–317 (2019).
87. B. Genç *et al.*, Upper motor neurons are a target for gene therapy and UCHL1 is necessary and sufficient to improve cellular integrity of diseased upper motor neurons. *Gene Ther.* **29**, 178–192 (2022).
88. X. Chen *et al.*, Intrathecal AAV9/AP4M1 gene therapy for hereditary spastic paraplegia 50 shows safety and efficacy in preclinical studies. *J. Clin. Invest.* **133**, e164575 (2023).
89. D. W. Huang, B. T. Sherman, R. A. Lempicki, Systematic and integrative analysis of large gene lists using DAVID bioinformatics resources. *Nat. Protoc.* **4**, 44–57 (2009).
90. B. T. Sherman *et al.*, DAVID: A web server for functional enrichment analysis and functional annotation of gene lists (2021 update). *Nucleic Acids Res.* **50**, W216–W221 (2022).